



This is a repository copy of *Modified shear stress transport model with curvature correction for the prediction of swirling flow in a cyclone separator*.

White Rose Research Online URL for this paper:
<http://eprints.whiterose.ac.uk/97729/>

Version: Accepted Version

Article:

Alahmadi, Y.H. and Nowakowski, A.F. (2016) Modified shear stress transport model with curvature correction for the prediction of swirling flow in a cyclone separator. *Chemical Engineering Science*, 147. pp. 150-165. ISSN 0009-2509

<https://doi.org/10.1016/j.ces.2016.03.023>

Article available under the terms of the CC-BY-NC-ND licence
(<https://creativecommons.org/licenses/by-nc-nd/4.0/>)

Reuse

This article is distributed under the terms of the Creative Commons Attribution-NonCommercial-NoDerivs (CC BY-NC-ND) licence. This licence only allows you to download this work and share it with others as long as you credit the authors, but you can't change the article in any way or use it commercially. More information and the full terms of the licence here: <https://creativecommons.org/licenses/>

Takedown

If you consider content in White Rose Research Online to be in breach of UK law, please notify us by emailing eprints@whiterose.ac.uk including the URL of the record and the reason for the withdrawal request.

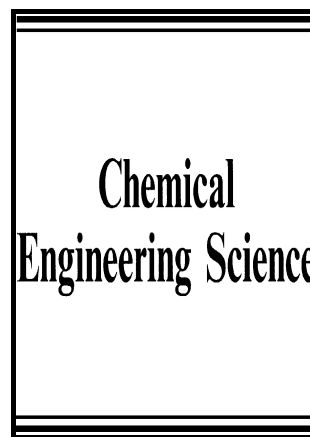


eprints@whiterose.ac.uk
<https://eprints.whiterose.ac.uk/>

Author's Accepted Manuscript

Modified shear stress transport model with curvature correction for the prediction of swirling flow in a cyclone separator

Yaser H. Alahmadi, Andrzej F. Nowakowski



www.elsevier.com/locate/ces

PII: S0009-2509(16)30121-X
DOI: <http://dx.doi.org/10.1016/j.ces.2016.03.023>
Reference: CES12859

To appear in: *Chemical Engineering Science*

Received date: 3 November 2015
Revised date: 6 March 2016
Accepted date: 13 March 2016

Cite this article as: Yaser H. Alahmadi and Andrzej F. Nowakowski, Modified shear stress transport model with curvature correction for the prediction of swirling flow in a cyclone separator, *Chemical Engineering Science* <http://dx.doi.org/10.1016/j.ces.2016.03.023>

This is a PDF file of an unedited manuscript that has been accepted for publication. As a service to our customers we are providing this early version of the manuscript. The manuscript will undergo copyediting, typesetting, and review of the resulting galley proof before it is published in its final citable form. Please note that during the production process errors may be discovered which could affect the content, and all legal disclaimers that apply to the journal pertain.

Modified shear stress transport model with curvature correction for the prediction of swirling flow in a cyclone separator

Yaser H. Alahmadi, Andrzej F. Nowakowski*

*Sheffield Fluid Mechanics Group SFMG, Department of Mechanical Engineering
The University of Sheffield, Sir Frederick Mappin Building, Mappin Street, Sheffield, S1 3JD, UK*

Abstract

The paper investigates the confined swirling flow in a cyclone. The numerical simulations are performed using a proposed eddy viscosity turbulence model, which accounts for the effects of the streamline curvature and rotation. This distinguishes the current model from the conventional Eddy Viscosity Models (EVMs) that are known to fail to predict the Rankine vortex in swirling flows. Although computationally more expensive approaches, the Reynolds Stress Model (RSM) and Large Eddy Simulation (LES), have demonstrated a high capability of dealing with such flows, these techniques are often unsuited for use in complex design studies where computational speed and robustness are key factors. In the present approach, the Shear Stress Transport with Curvature Correction (SSTCC) turbulence model is modified by the introduction of the Richardson number to account for the rotation and curvature effects. The numerical predictions were validated using experimental results and also compared to the data obtained using the RSM model and various EVMs without the proposed modifications. The investigations started with a benchmark case of a flow through a channel duct with a U-turn, after which more challenging simulations of a high swirling flow within a cyclone separator device were performed. The results show that the proposed model is competitive in terms of accuracy when compared to RSM and proves to be superior to the RSM model in terms of computational cost. Furthermore, it is found that the proposed model preserves the ability to represent the Rankine vortex profile at different longitudinal levels of the cyclone. It is also more efficient in terms of the computational cost than the SSTCC model without the introduced modifications.

Keywords: Swirling Flows, Computational Fluid Dynamics, Cyclone Separator, Eddy Viscosity Model

1. Introduction

Vortex and swirling flows occur in a wide range of different mechanical apparatus, for instance, in dust collection devices, spray dryers, vortex tubes and combustion chambers. In addition, vortices and swirling flows are commonly encountered in nature in atmospheric phenomena, such as tornadoes and dust devils. A superb prologue to the swirling flows found in nature and in technology is given by Lugt [1].

A cyclone separator is a fixed and stationary mechanical device that separates dispersed solid particles from a carrier gas stream by employing a centrifugal force. The tangential inlet at the top of the device plays an important role in the mechanism and working principle of the cyclone. The dimensions of the inlet and the vortex finder cause the flow to descend in a spiral motion. This creates a centrifugal force that deposits the solid particles onto the cyclone body wall, after which the particles spiral down with the descending flow. At the end of the conical part of the cyclone, the solid particles are trapped at the hopper section or are discharged via an apex exit (see Fig. 1). The gas phase reverses and ascends axially in a spiral motion at the core of the cyclone and exits through the upper exit pipe.

Cyclones are common in many (heavy or light) industrial applications and they are designed as classifiers or separators. Their widespread presence is due to several factors, among which the complete absence of moving parts, the low maintenance cost, the low running cost and the simple geometry are considered as crucial.

A large number of numerical and experimental studies have been conducted to investigate the flow within the cyclone. The majority of the numerical simulations were performed by using either the turbulent resolving approaches (Large Eddy Simulation (LES) or Detached Eddy Simulation (DES)) or the Reynolds Stress Model (RSM) [2]. It should be noted

*corresponding author

Email address: a.f.nowakowski@sheffield.ac.uk (Andrzej F. Nowakowski)

that the flow within the cyclone is characterized as a strong swirling flow with a strong streamline curvature. In this scenario, the conventional Eddy Viscosity Models (EVMs) fail to predict the effects of strong streamline curvatures. This is unfortunate, as the robustness and computational cost of the EVMs are superior to RSM [3, 4].

It is well known that a major drawback of the EVMs is their incapacity to capture the effects resulting from the rotating system. More specifically, if the flow exhibits a swirl motion, EVMs fail to represent the near wall region "free-loss vortex" part of the Rankine vortex. This is attributed to the use of the Boussinesq hypothesis that assumes that the eddy viscosity is an isotropic scalar which is untrue for more complex flows such as cyclones. In order to handle this weakness, many modifications aimed at the sensitization of EVMs to rotation and curvature have been suggested (see Refs. [5, 6, 7]). These attempts are limited and not universal, especially when dealing with 3D flows. Moreover, these corrections are not Galilean-invariant. In 1997, Spalart and Shur [8] proposed an empirical alteration to EVMs to account for the system of rotation and streamline curvature, which in a sense is close to an idea of Knight and Saffman [9]. The former is more efficient as it measures the extra influence of the invariant contributor to the turbulence. It is also relatively easy to apply to 3D flows and unifies the description of the curvature and rotation effects in the mathematical model. Also in 1997, Hellsten [10] proposed some improvement to the well known $k - \omega$ SST turbulence model. The modification included the sensitization for the effects of system rotation and streamline curvature. Among several different definitions of Richardson number (Ri), Hellsten realisation replaces the turbulent time scale appearing in the Khodak and Hirsch [11] definition by the mean-flow time scale $1/S_{ij}$. This results in a new and simple definition of the Ri number which can be written as follows

$$Ri = \frac{\Omega_{ij}}{S_{ij}} \left(\frac{\Omega_{ij}}{S_{ij}} - 1 \right) \quad (1)$$

By 2009, Smirnov and Menter [3] had adapted the rotation-curvature correction function proposed earlier in [8] to the shear stress transport $k - \omega$ model (SST $k - \omega$). The correction function was applied to the production term in both the k and ω transport equa-

tions. As a result, the corrected model, denoted as the SSTCC, becomes more accurate, computationally efficient and robust than its predecessor. In 2013, a new simpler rotation and curvature correction method for the S-A model was proposed by Zhang and Yang [12]. These modifications avoid the calculations of the components of the Lagrangian derivatives of the strain rate tensor (DS_{ij}/Dt) by implementing Ri number. The model is denoted as SARCM, where the M stands for modified.

In this work, the definition of Ri number suggested by Hellsten is used to avoid the need to calculate the complex term (DS_{ij}/Dt), that appears in the non-dimensional argument \tilde{r} . This leads to a simpler version of the SSTCC, which is realized by implementing the Ri number. As a result, the obtained numerical code requires less computational time and is also competitive in terms of accuracy when compared to the RSM model. The new formula for \tilde{r} is applied into the rotation function developed in [3]. The proposed model is denoted as SSTCCM. Then, the two altered models, namely (SARCM and SSTCCM) and the conventional $k - \omega$ SST model, are implemented to study the flow within the cyclone. The swirl velocity components characterized by the tangential and axial velocity profile are compared with RSM and experimental data.

The paper is organized as follows. Section 2 provides a brief introduction to the swirling flow inside cyclones. The physical and analytical description of the vortex pattern is revisited. Section 3 describes the governing equations and turbulence modelling, which is followed by an explanation of the numerical implementation of the proposed approach. The results of the computational work are presented in section 5. First, a U-duct problem is utilized for verification and validation studies. Then, a Stairmand cyclone model is numerically investigated to demonstrate the capabilities of the proposed formulation in a swirling flow regime. The conclusion is presented in section 6.

2. Swirl flow in cyclones

The behaviour of the swirling flow can be defined as a combination of the tangential velocity component with the axial one. When real swirling flow problems are analyzed in a

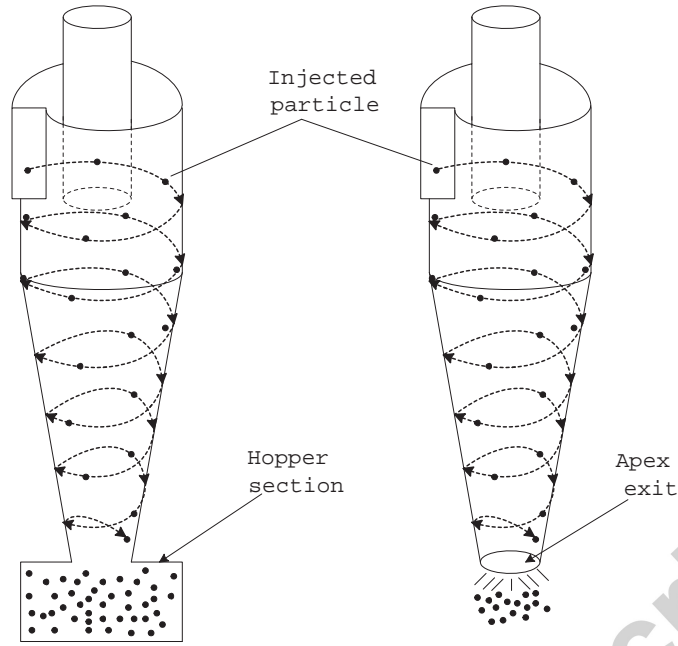


Figure 1: Motion of collected particles inside cyclone separator.

confined domain, the tangential velocity component of such flows is bounded with two limiting regimes; namely the solid body rotation and the free vortex [13]. The aforementioned type is also known as a forced vortex flow. By assuming that the fluid behaves like a solid body or has infinite viscosity, the angular velocity of a fluid element remains constant at different radial positions. Hence, a swirling flow with a constant angular velocity is called the forced vortex flow or in the other context, solid-body rotation, so that:

$$v_{\theta} = \Omega r \quad (2)$$

Where v_{θ} is the tangential velocity, Ω is the angular velocity and r is the radial position. The second extreme contrasts with the forced vortex flow, where the fluid has no viscosity. In this case, the motions of the fluid elements at all radial positions do not influence each other in any way. For such a fluid, the relation between the radial position and the tangential velocity is inversely proportional. Therefore, as the fluid element moves toward the center of the circulation, its tangential velocity increases. This relation can be referred to as the conservation of the moment-of-momentum (mass times tangential velocity times radius of rotation: $mv_{\theta}r$). As the moment-of-momentum is conserved, the quantity $mv_{\theta}r$ is constant.

This implies that $v_{\theta}r = \text{constant}$ for a mass conserved fluid element, so that:

$$v_{\theta} = \frac{\text{constant}}{r} \quad (3)$$

This limiting frictionless case is represented by (3). This equation demonstrates that the tangential velocity increases as the fluid element moves toward the center of the rotation.

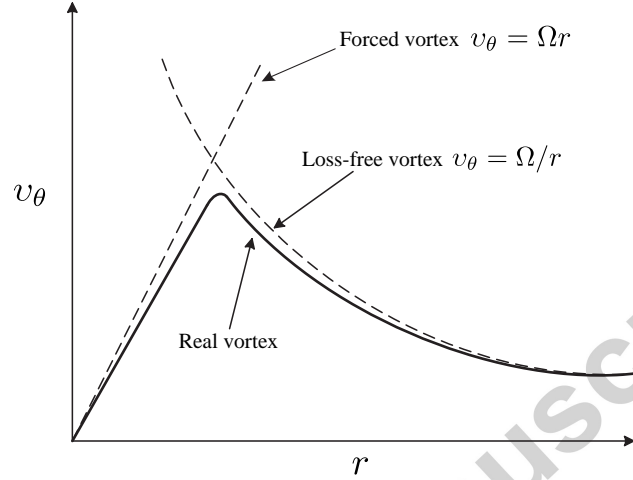


Figure 2: Tangential velocity distribution of the two extremes vortex flows and a real vortex flow.

As shown in Fig. 2, the swirl flow acts as an intermediary between the solid-body rotation and the loss free vortex. In real fluid, the viscous effects and the presence of turbulence are the two main sources that cause the transportation of the moment-of-momentum between the fluid elements at different radii [14]. Thus, in the inner core region, the tangential velocity of the swirling flow nearly matches that of the solid-body rotation. This inner core is surrounded by a nearly loss free vortex. The tangential velocity distribution which acts as an intermediary between these two extremes is known as the "Rankine vortex".

Further, to understand fully the mechanism of the cyclone, it is necessary to understand the flow behaviour of the gases within it. In 1939, Shepherd and Lapple [15], investigated experimentally the velocity profile of the flow inside the cyclone. Their investigation has shown that the flow within the cyclone consists primarily of two flow regimes. The first regime is an outer downward spiral while the other is an inner upward spiral with lower velocity and smaller diameter, as shown in Fig. 3.

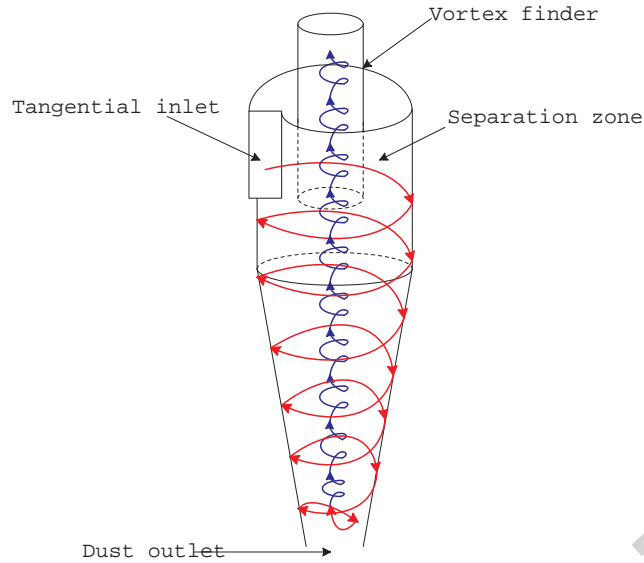


Figure 3: Sketch of the flow pattern inside cyclone separator.

The outer downward flow is of a great importance as it is responsible for transporting the solid particles toward the cyclone wall. These flow patterns are known as 'the outer vortex and the inner vortex'. The fluid transfers from the outer vortex to the inner vortex. The transfer process starts just below the vortex finder down through the conical part to a point close to the apex of the cyclone. The measurement of Ter Linden [16] showed that in the upper part of the cyclone, the cylindrical part, the inner and outer vortex interface at a radius that is approximately equal to the radius of the vortex finder. The gas flow in the cyclone is, by nature, a three-dimensional flow and is mainly dominated by the tangential velocity and strong shear.

The second velocity component which plays a major role in the reverse flow cyclone is the axial velocity component of the underlying gas flow. For instance, the transportation of the solid particles toward the apex of the cyclone is influenced mainly by the axial velocity rather than the gravitational force. In the outer vortex region (the near wall region), the direction of the axial velocity is downward and the gas moves toward the apex, while for the inner vortex region (the near centre line region) the direction is upward and the gas moves toward the vortex finder [17]. Figure 4 provides a sketch of the axial velocity profile where

the near wall flow is presented in a negative direction to indicate that the flow is moving downward, while near the center or the core of the cyclone is represented by a positive direction to indicate that the flow is moving upward.

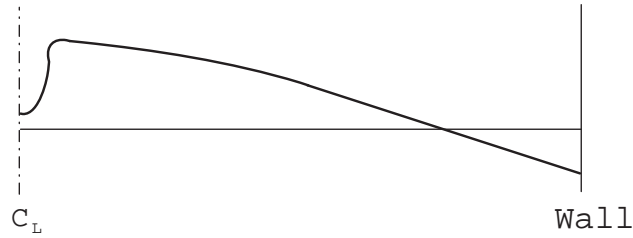


Figure 4: Sketch of the axial velocity profile in cyclone separators.

It is argued that the vortex finder diameter has the major influence on the axial velocity profile. Figure 5 shows two different patterns of the axial velocity profile, namely, the inverted V pattern to the left and the inverted W pattern to the right. Both profiles are taken at the same horizontal position below the vortex finder. For smaller vortex finder diameters, the axial velocity profile is more likely to take the form of the inverted V pattern, and for larger diameters, it turns into the inverted W pattern. The phenomenon of the shift in the axial velocity profile between these two patterns as the vortex diameter changes was investigated by Horvath et al. [18], who studied the effect of the size of the vortex finder on the axial velocity profile. They observed that, when the dimensionless diameter of the vortex finder D_x/D is less than 0.45, the axial velocity has a stable V pattern profile. For higher ratios of D_e/D , this pattern is unstable, and only when the ratio is greater than 0.53, stable W pattern is observed. This is a consequence of a low pressure zone occurring at the core of the vortex, that leads to an increase in the back flow and of the air from outside to the core, hence, a W pattern is more stable for larger vortex diameter. These characteristics of the swirling flow pattern constitute a challenge when designing a turbulence model for practical applications.

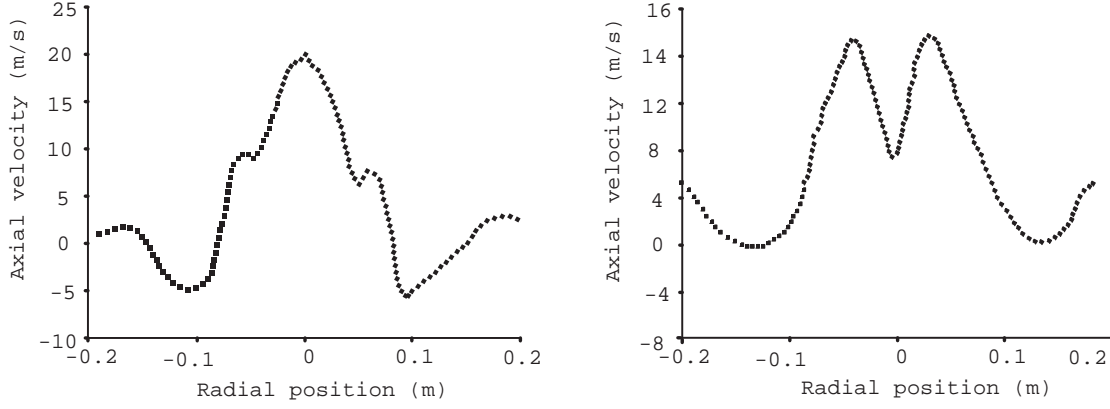


Figure 5: The axial velocity profile in cyclone separators the inverted V pattern on the left and the inverted W pattern on the right [18].

3. Governing equations and turbulence modelling

Cyclone separators operate normally at a range of $Re = 10^5$ to 10^6 . Such a flow is considered to be fully turbulent. The fundamental physics of the fluid flow is described and governed mathematically by the Navier-Stokes equations. The conservation forms of the incompressible Navier-Stokes equations are given by the continuity and momentum equation, respectively:

$$\frac{\partial u_i}{\partial x_i} = 0 \quad (4)$$

$$\rho \frac{\partial u_i}{\partial t} + \rho \frac{\partial u_i u_j}{\partial x_j} = -\frac{\partial p}{\partial x_i} + \frac{\partial}{\partial x_j} (2\mu s_{ij}) \quad (5)$$

where u and p have their usual meaning of velocity and pressure, and the term s_{ij} is the strain-rate tensor, which is written as:

$$s_{ij} = \frac{1}{2} \left(\frac{\partial u_i}{\partial x_j} + \frac{\partial u_j}{\partial x_i} \right) \quad (6)$$

The flow variables in equations (4) and (5) are decomposed into mean and fluctuating quantities. Then the time average process is applied, which yields the final form of the Reynolds averaged Navier-Stokes equations that can be written as follows:

$$\frac{\partial \bar{u}_i}{\partial x_i} = 0 \quad (7)$$

$$\rho \frac{\partial \overline{u_i}}{\partial t} + \rho \frac{\partial \overline{u_i u_j}}{\partial x_j} = -\frac{\partial \overline{p}}{\partial x_i} + \frac{\partial}{\partial x_j} (2\mu S_{ij} - \overline{\rho u_i' u_j'}) \quad (8)$$

where the term S_{ij} is the time averaged quantity of the strain-rate tensor. The appearance of the additional term ($\tau_{ij} = -\overline{\rho u_i' u_j'}$) is known as the Reynolds stress tensor. The system of the equations has to be closed in order to find a solution to the mathematical problem. This can be achieved by postulating a specific term of τ_{ij} in a framework of designing a turbulence model.

3.1. Standard Spalart-Allmaras (SA) turbulence model

The standard SA turbulence model was presented first by Spalart and Allmaras in 1992 [19]. It is a one-equation turbulence model. The SA model employs the Boussinesq hypothesis to relate the Reynolds stresses to the mean rate of deformation.

$$\tau_{ij} = -\overline{\rho u_i' u_j'} = 2\mu_t S_{ij} = 2\nu_t \rho S_{ij} = \rho \tilde{\nu} f_{v1} \left(\frac{\partial \overline{u_i}}{\partial x_j} + \frac{\partial \overline{u_j}}{\partial x_i} \right) \quad (9)$$

The transport equation for the viscosity-like variable $\tilde{\nu}$ is given by

$$\frac{\partial}{\partial t}(\rho \tilde{\nu}) + \frac{\partial}{\partial x_i}(\rho \tilde{\nu} u_i) = c_{b1} \rho \tilde{S} \tilde{\nu} + \frac{1}{\sigma} \left[\frac{\partial}{\partial x_j} \left\{ (\mu + \rho \tilde{\nu}) \frac{\partial \tilde{\nu}}{\partial x_j} \right\} + c_{b2} \rho \left(\frac{\partial \tilde{\nu}}{\partial x_j} \right)^2 \right] - Y_\nu \quad (10)$$

where

$$\nu_t = \tilde{\nu} f_{v1}, \quad f_{v1} = \frac{\chi^3}{\chi^3 + c_{v1}^3}, \quad \chi = \frac{\tilde{\nu}}{\nu}, \quad \tilde{S} \equiv \Omega + \frac{\tilde{\nu}}{\kappa^2 d^2} f_{v2} \quad (11)$$

Where $\Omega \equiv \sqrt{2\omega_{ij}\omega_{ij}}$ is the magnitude of the vorticity, d is the distance from the field point to the nearest wall and ω_{ij} is the mean rate-of-rotation tensor, defined by:

$$\omega_{ij} = \frac{1}{2} \left(\frac{\partial u_i}{\partial x_j} - \frac{\partial u_j}{\partial x_i} \right) \quad (12)$$

The destruction of turbulent viscosity that occurs in the near-wall region due to wall blocking and viscous damping is given by:

$$Y_\nu = c_{w1} \rho f_w \left(\frac{\tilde{\nu}}{d} \right)^2 \quad (13)$$

The f_w function is used to accelerate the decaying behaviour of destruction and it is given by

$$f_w = g \left(\frac{1 + c_{\omega 3}^6}{g^6 + c_{\omega 3}^6} \right)^{1/6} \quad (14)$$

In order to prevent a large value of f_w a limiter function g is used

$$g = r + c_{\omega 2} (r^6 - r) \quad (15)$$

Where r is defined as

$$r \equiv \frac{\tilde{\nu}}{\tilde{S} \kappa^2 d^2} \quad (16)$$

The eight constant closure coefficients of the SA model are given in Table 1.

Table 1: Spalart-Allmaras closure constants.

| κ | c_{v1} | c_{b1} | c_{b2} | σ | c_{w1} | c_{w2} | c_{w3} |
|----------|----------|----------|----------|----------|----------|----------|----------|
| 0.4187 | 7.1 | 0.1355 | 0.622 | 2/3 | 3.2059 | 0.3 | 2.0 |

3.2. Zhang and Yang's simpler SARC turbulence model

As the standard SA model does not account for system rotation and streamline curvatures, Spalart and Shur [8] proposed an empirical alteration for this purpose. The formulation of SARC is similar to the original standard SA model except that the production term of turbulence viscosity in equation (10) is multiplied by a rotation function f_{r1} , which is given by:

$$f_{r1}(r^*, \tilde{r}) = (1 + c_{r1}) \frac{2r^*}{1 + r^*} [1 - c_{r3} \tan^{-1}(c_{r2} \tilde{r})] - c_{r1} \quad (17)$$

The calculation of the Lagrangian derivative of the strain rate tensor that exists in the SARC mode is a complex term and time consuming to implement. Thus, in order to avoid the calculation of the higher order derivatives, Zhang and Yang [12] implemented

the Richardson number Ri and redefined the argument (\tilde{r}) proposed in [8]. Therefore, the parameters r^* and \tilde{r} are given by:

$$r^* = \frac{S}{\Omega} \quad (18)$$

$$\tilde{r} = \frac{\Omega}{S} \left(\frac{\Omega}{S} - 1 \right) \quad (19)$$

Here

$$S_{ij} = 0.5 \left(\frac{\partial u_i}{\partial x_j} + \frac{\partial u_j}{\partial x_i} \right), \quad \omega_{ij} = \left(0.5 \left(\frac{\partial u_i}{\partial x_j} - \frac{\partial u_j}{\partial x_i} \right) + 2\varepsilon_{mji}\Omega_m \right) \quad (20)$$

$$S = \sqrt{2S_{ij}S_{ij}}, \quad \Omega = \sqrt{2\omega_{ij}\omega_{ij}}, \quad (21)$$

The empirical constants c_{r1} , c_{r2} and c_{r3} that appear in equation (17) are given the values 1.0, 2.0 and 1.0, respectively.

3.3. Smirnov and Menter SSTCC model

The shear stress transport model is an improved version of the two equations $k-\omega$ model. It was introduced in 1994 by F.R. Menter [20]. The model combines the two turbulence models ($k-\omega$ and $k-\epsilon$). In the inner part of the boundary layer, the $k-\omega$ model is used and switches to the $k-\epsilon$ in the free shear flow. The SST model employs the Boussinesq hypothesis to relate the Reynolds stresses to the mean rate of deformation as follows:

$$\tau_{ij} = -\rho \overline{u'_i u'_j} = \mu_t \left(2S_{ij} - \frac{2}{3} \frac{\partial u_k}{\partial x_k} \delta_{ij} \right) - \frac{2}{3} \rho k \delta_{ij} \quad (22)$$

The conservation form of the transport equations for both the turbulence kinetic energy k and the turbulent frequency ω can be written as:

$$\rho \frac{\partial(k)}{\partial t} + \rho \frac{\partial(u_j k)}{\partial x_j} = P_k - \beta^* \rho k \omega + \frac{\partial}{\partial x_j} \left[(\mu + \sigma_k \mu_t) \frac{\partial k}{\partial x_j} \right] \quad (23)$$

$$\rho \frac{\partial(\omega)}{\partial t} + \rho \frac{\partial(u_j \omega)}{\partial x_j} = P_k \frac{\rho}{\mu_t} - \beta \rho \omega^2 + \frac{\partial}{\partial x_j} \left[(\mu + \sigma_\omega \mu_t) \frac{\partial \omega}{\partial x_j} \right] + 2(1 - F_1) \frac{\rho \sigma_{\omega 2}}{\omega} \frac{\partial k}{\partial x_j} \frac{\partial \omega}{\partial x_j} \quad (24)$$

The production term P_k is defined as:

$$P_k = \tau_{ij} \frac{\partial u_i}{\partial x_j} = \left[\mu_t \left(2S_{ij} - \frac{2}{3} \frac{\partial u_k}{\partial x_k} \delta_{ij} \right) - \frac{2}{3} \rho k \delta_{ij} \right] \frac{\partial u_i}{\partial x_j} \quad (25)$$

where the turbulent viscosity is defined as follows:

$$\mu_t = \frac{\rho a_1 k}{\max(a_1 \omega, \Omega F_2)} \quad (26)$$

The blending function F_1 in the freestream is zero ($k-\varepsilon$ model), and in the boundary layer is equal to one ($k-\omega$ model), given by:

$$F_1 = \tanh(arg_1^4) \quad (27)$$

$$arg_1 = \min \left[\max \left(\frac{\sqrt{k}}{\beta^* \omega d}, \frac{500\nu}{d^2 \omega} \right), \frac{4\rho \sigma_{\omega 2} k}{CD_{k\omega} d^2} \right] \quad (28)$$

$$CD_{k\omega} = \max \left(2\rho \sigma_{\omega 2} \frac{1}{\omega} \frac{\partial k}{\partial x_j} \frac{\partial \omega}{\partial x_j}, 10^{-20} \right) \quad (29)$$

$$F_2 = \tanh(arg_2^2) \quad (30)$$

$$arg_2 = \max \left(2 \frac{\sqrt{k}}{\beta^* \omega d}, \frac{500\nu}{d^2 \omega} \right) \quad (31)$$

The constant closure coefficients of the SST model are given in Table 2.

Table 2: SST $k-\omega$ closure constants.

| κ | σ_k | σ_ω | $\sigma_{\omega 2}$ | β_1 | β_2 | β^* | a_1 |
|----------|------------|-----------------|---------------------|-----------|-----------|-----------|-------|
| 0.4187 | 0.85 | 0.5 | 0.856 | 0.0785 | 0.0828 | 0.09 | 0.31 |

Smirnov and Menter [3] modified the rotation function equation (17) which was proposed by Spalart and Shur [8]. The rotation function was applied to control the production term of the original two equation SST model. Hence, the kinetic energy equation in the original SST model is modified as follows:

$$\frac{\partial(\rho k)}{\partial t} + \frac{\partial(\rho u_j k)}{\partial x_j} = P_k f_{rot} - \beta^* \rho k \omega + \frac{\partial}{\partial x_j} \left[\mu_{ef} \frac{\partial k}{\partial x_j} \right] \quad (32)$$

and the specific dissipation rate in the original SST model is modified as follows:

$$\frac{\partial(\rho \omega)}{\partial t} + \frac{\partial(\rho u_j \omega)}{\partial x_j} = \alpha \frac{\rho P_k}{\mu_t} f_{rot} - D_\omega + C d_\omega + \frac{\partial}{\partial x_j} \left[\mu_{ef} \frac{\partial \omega}{\partial x_j} \right] \quad (33)$$

The rotation function f_{rot} is defined as

$$f_{rot} = \max \{ \min (f_{r1}, 1.25), 0.0 \} \quad (34)$$

The term f_{r1} is the rotation function defined in equation (17). Unlike the production term in SA model equation (10), which is based on the vorticity tensor Ω that characterizes the rotation, the production term P_k is based on the strain tensor rate S that characterizes the deformation, and hence P_k is higher than \tilde{S} , which justify the use of the limiter in the rotating function f_{rot} [3]. Further modification is applied to the dimensionless quantity \tilde{r} and redefined as follows:

$$\tilde{r} = \frac{2\omega_{ik} S_{jk}}{D^3 \Omega} \left(\frac{DS_{ij}}{Dt} + (\varepsilon_{imn} S_{jn} + \varepsilon_{jmn} S_{in}) \Omega_m \right) \quad (35)$$

where DS_{ij}/Dt is the Lagrangian derivative and the term D is given by:

$$D = \sqrt{0.5(S^2 + \Omega^2)} \quad (36)$$

3.4. The proposed SSTCCM model

The present model builds on the shear stress transport $k - \omega$ model (SST $k - \omega$) and also on the rotation function which was proposed in [3]. In the proposed model, the Richardson number Ri defined by Hellsten [10] is used to avoid calculating the terms D^3 and the complex

Lagrangian derivatives. The modified rotation function is used to control the production term that appears in the transport equations. The incompressible form of the transport equations of the turbulent kinetic energy and its specific dissipation for the new SSTCCM model are exactly the same as those given by equations (32) and (33). The dimensionless quantities \tilde{r} and r^* are defined as follows

$$\tilde{r} = \frac{\Omega}{S} \left(\frac{\Omega}{S} - 1 \right) \quad r^* = \frac{S}{\Omega} \quad (37)$$

The recommended boundary conditions for the farfield and at the wall for this model are given in Table 6. Table 3 summarize the implemented sensitized EVMs.

Table 3: Different sensitization of turbulence models to rotation and curvature.

| Models | Rotation function | r^* argument | \tilde{r} argument |
|--------|---------------------------------|--------------------|--|
| SARC | f_{r1} | $\frac{S}{\Omega}$ | $\frac{2\omega_{ik}S_{jk}}{D^4} \left(\frac{DS_{ij}}{Dt} \right)$ |
| SARCM | f_{r1} | $\frac{S}{\Omega}$ | $\frac{\Omega}{S} \left(\frac{\Omega}{S} - 1 \right)$ |
| SSTCC | $\max(\min(f_{r1}, 1.25), 0.0)$ | $\frac{S}{\Omega}$ | $\frac{2\omega_{ik}S_{jk}}{D^4} \left(\frac{DS_{ij}}{Dt} \right)$ |
| SSTCCM | $\max(\min(f_{r1}, 1.25), 0.0)$ | $\frac{S}{\Omega}$ | $\frac{\Omega}{S} \left(\frac{\Omega}{S} - 1 \right)$ |

4. Numerical implementation and simulation setup

4.1. Solver and algorithm

The turbulence model discussed in Section 3 was implemented using the open source OpenFoam-2.4.0 numerical platform [21]. The ease of accessing and modifying the platform code facilitated the implementation of the proposed equations. The incompressible turbulent

$U = 31.1$ m/s represents the mean velocity at the inlet. The characteristic length L is the width of the duct ($L = H = 0.0381$ m).

Table 4: Set up of the U-duct boundary conditions.

| Boundary | \mathbf{u} (m/s) | p (m ² /s ²) | k (m ² /s ²) | omega (1/s) | ν_t (m ² /s) |
|----------|--------------------|---------------------------------------|---------------------------------------|--------------------------------------|-----------------------------|
| Inlet | $(u_x, 0, 0)$ | zero gradient | $\frac{2}{3}(I^*U)^2$ | $\frac{5U}{L}$ | $\frac{k}{omega}$ |
| Outlet | zero gradient | 0 | zero gradient | zero gradient | zero gradient |
| Wall | $(0, 0, 0)$ | zero gradient | 0 | $10\frac{6\nu}{\beta_1(\Delta y)^2}$ | 0 |

*The turbulent intensity ($I = 0.16Re^{-0.125}$).

4.3. Grid generation and numerical setting for the 3D cyclone

The computational cost as well as the accuracy of the solution depend on the quality of the computational grid. The meshing technique can employ a fully structured, unstructured or hybrid grid. The discretisation error arises due to the size and shape of the grid cells, while the numerical complexity depends on the grid resolution (the number of cells) and the quality of the mesh. The meshing of the complex geometries, such as those representing cyclones, is challenging and the fully structured grids which are generally preferred require some extra treatment. The body of a cyclone consists of three dissimilar geometrical shapes, which are a conical frustum, a circular cylinder and a rectangular prism. The way in which these shapes are attached to form the cyclone body makes the meshing process using fully structural hexahedrals extremely difficult. For example, even for a coarse mesh, this would yield a very dense grid area around the symmetry-axis, on the one hand, and high non-orthogonal faces on the other hand (see Fig. 7). For medium and fine grids, both the dense grid area and the level of the non-orthogonality increase dramatically. To handle this problem in the simulations presented in Section 5.2, the non-orthogonal corrector which forms a part of the PIMPLE algorithm is applied to rectify the calculations and consequently to improve the

accuracy. This procedure is realised on the mesh produced using an open source Gmsh-2.8.6 code [23].

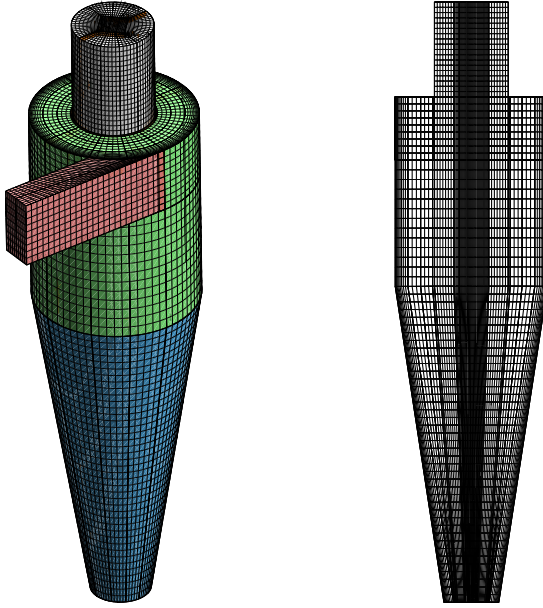


Figure 7: Structured grid generated by Gmsh. From left to right, the block-mesh based on the geometrical shape, cross-section along the z-axis and the location of the non-orthogonal faces.

Three numerical simulations were carried out based on different grid sizes. Table 5 summarizes the selection of meshes used for the grid independence study. The listed error constitutes the difference between two refinements. It is calculated as a measure of the accuracy of the coarser of two successive grids. It is found that the finest grid makes an insignificant improvement in predicting the dimensionless pressure drop (Euler number), but produces a large number of non-orthogonal faces. These faces unnecessarily increase the computational effort as they require additional non-orthogonal correctors in the internal loop within each time step. All of the numerical results presented in section (5.2) are performed through the application of the medium grid size.

In this work, the flow inside a Stairmand high efficiency cyclone was simulated. The cyclone geometry major design parameters are presented in Fig. 8 and Table 6. The Reynolds number for this case based on the characteristic length L representing the cyclone body di-

Table 6: Geometry of the high efficiency Stairmand cyclone design.

| Dimension | Stairmand |
|-------------------------------|-----------|
| Cyclone diameter, D | 0.29 m |
| Gas outlet diameter, D_x/D | 0.5 |
| Dust outlet diameter, B_c/D | 0.375 |
| Inlet height, a/D | 0.5 |
| Inlet width, b/D | 0.2 |
| Outlet duct length, S/D | 0.5 |
| Cylinder height, h/D | 1.5 |
| Cyclone height, H/D | 4.0 |

$$\mathbf{u} = (u_x, 0, 0) \quad (\text{inlet}) \qquad \mathbf{u} = (0, 0, 0) \quad (\text{fixed wall}) \qquad (38)$$

Neumann boundary conditions [24] are applied at both outlets. All boundary conditions, which include the pressure and the turbulent quantities, are summarized in Table 7.

Table 7: Set up of the cyclone boundary conditions.

| Boundary | \mathbf{u} (m/s) | p (m^2/s^2) | k (m^2/s^2) | omega (1/s) | ν_t (m^2/s) |
|---------------|--------------------|---------------------------------|---------------------------------|---------------------------------------|-----------------------------------|
| Inlet | $(u_x, 0, 0)$ | zero gradient | $\frac{2}{3}(IU)^2$ | $\frac{5U}{L}$ | $\frac{k}{\omega}$ |
| Top outlet | zero gradient | 0 | zero gradient | zero gradient | zero gradient |
| Bottom outlet | zero gradient | 0 | zero gradient | zero gradient | zero gradient |
| Wall | $(0, 0, 0)$ | zero gradient | 0 | $10 \frac{6\nu}{\beta_1(\Delta y)^2}$ | 0 |

5. Results and discussion

The obtained predictions are compared with the Laser Doppler Anemometry (LDA) experimental measurements and with the corresponding results of the RSM. Both the experiment and the RSM data were reported in [25]. In order to validate the new SSTCCM model, a simple benchmark problem of a U-duct case was implemented and simulated first. The motivation behind this verification test was to demonstrate the ability of the proposed model to tackle a strong streamline curvature, which proved to be a challenge for EVM models. This test has a relatively, compared to the cyclone, quicker turnaround time which allowed a wider selection of turbulence models to be tested first. As a result, the candidates models were identified for the following cyclone simulations.

5.1. Flow in a U-duct channel

Along with the proposed model, the flow is also simulated by the use of the original and the modified one-equation SA models, as well as the two-equations SST, $k - \omega$ and $k - \varepsilon$ models. The experimental measurements for the same geometry were reported in [26]. The numerical results are summarized in Fig. 10. They demonstrate the velocity profile within the U-duct at three cross-sectional positions; at the entrance of the bend $\theta = 0^\circ$, at the midway of the bend $\theta = \pi/2$ and at the end of the bend $\theta = \pi$.

As the flow passes the bend, the adverse pressure gradient is developed due to the curvature. At the upstream end of the bend, the lateral pressure gradient decreases, which in turn creates a massive separation zone near the inner wall. The prediction of this zone is challenging for the conventional EVMs turbulence models. The formation of the flow separation is visualized in Fig. 9 for different EVM models, with and without the rotation correction function. Table 8 summarizes the length of the separation zone which starts at position π as indicated in Fig. 6. Only the models sensitized to rotation-curvature corrections successfully capture the length of this separation zone.

The flow behavior encounters a dramatic changes as it passes through the bend. For example, in the first half of the bend, from $\theta = 0$ deg to $\theta = \pi/2$, the flow accelerates near the inner-wall and decelerates as it moves toward the outer-wall. As a result, the velocity

k-epsilon

SST

k-omega

SSTCC

SARCM

SSTCCM

Figure 9: Contour plots of the mean velocity of the flow within the U-duct for different EVM models.

profile at the entrance of the bend is more likely to form an asymmetric pattern. Figure 10a demonstrates that all of the EVM models accurately predict the velocity profile and also shows a lack of any significant advantages of the sensitized models over the conventional ones. This is expected, as the velocity measurements are collected before the bend entry. Figure 10b (halfway through the bend) demonstrates the extreme situation of the asymmetric pattern of the velocity profile, where the velocity reaches its minimum value near the outer wall and maximum value near the inner wall. In the second half of the bend, from $\theta = \pi/2$ to $\theta = \pi$, the curvature has a tremendous impact on the turbulence. Moreover, the flow pattern starts to reverse, and thus the velocity decreases near the inner wall and increases near the outer wall. The effects of the curvature on the flow field cannot be predicted by the conventional EVMs. This can obviously be observed in Fig. 10c, where the conventional EVMs underestimated the velocity profile near the outer and inner wall. On the other hand, the SSTCCM model accounts for the effects of the curvature of the inner and outer walls better than the conventional models. There is also a small difference observed between SSTCCM and SSTCC in Fig. 10c suggesting that the SSTCCM model is slightly advantageous in terms of accuracy. Although the models gave almost the same results for the velocity profiles and other variables analysed in various positions of the bend.

Figures. 11 and 12 show the Reynolds shear stress, $\overline{u'v'}$, and the corresponding turbulent kinetic energy, k , at the selected positions, as in the velocity profile figures. It should be noted that k data are not provided for the SARCM models, because the value is not explicitly computed in the SA turbulence model. The inner (convex) and outer (concave) curvatures have had significant impacts on the turbulence quantities. While the convex curvature causes a reduction in the turbulence quantities, the concave surface causes the opposite effects, increasing both the $\overline{u'v'}$ and k near the outer wall. This can be seen clearly at position $\pi/2$, which is the midpoint of the bend. Although the velocity profiles at this position for all of the conventional EVMs are in a good agreement with the experimental data, none of the models predict the turbulence quantities near the inner and outer walls. However, the SSTCC and SSTCCM model make significant improvements and shows the ability to account for the strong curvature of both the inner and outer walls. In addition, the sensitized

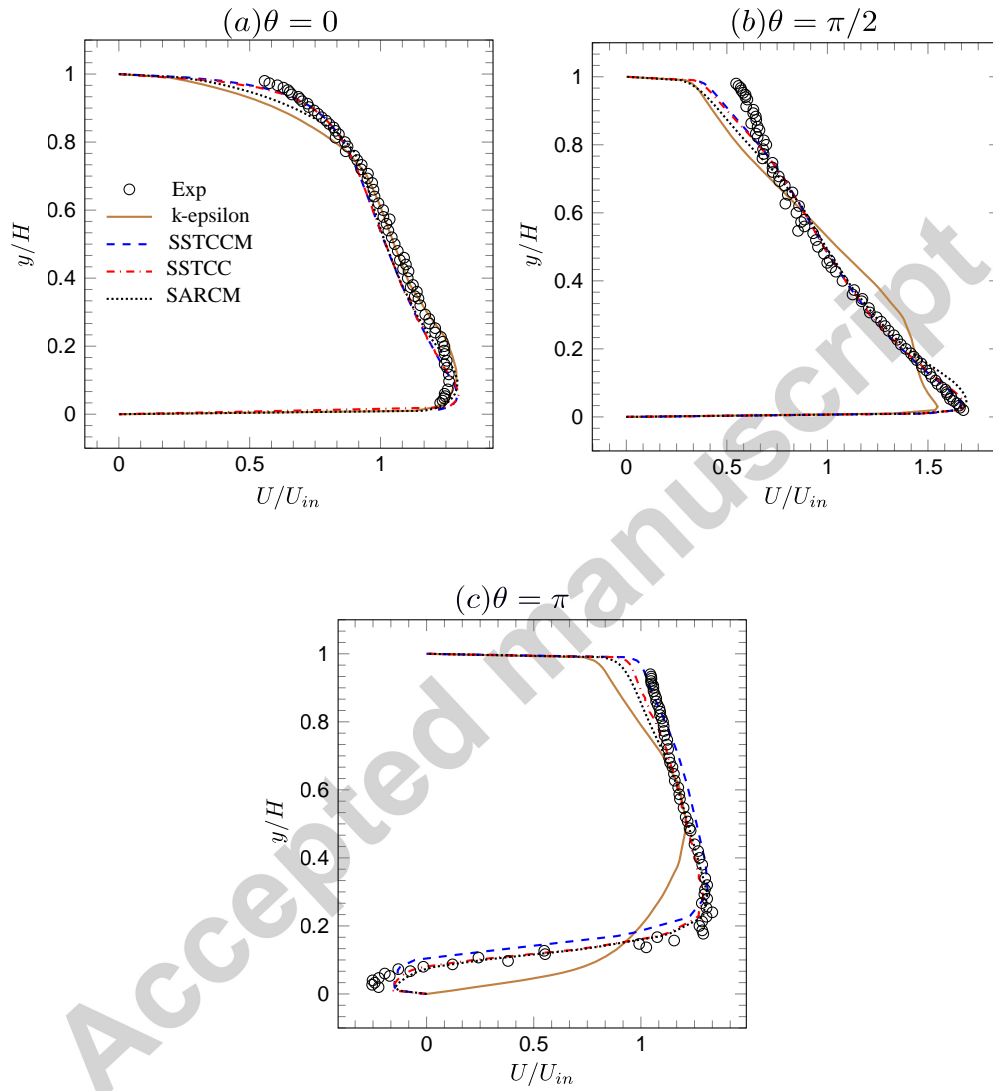


Figure 10: Velocity profile at $\theta = 0$, $\theta = \pi/2$ and $\theta = \pi$; comparison between the EVMs simulation and the LDA measurements.

models predict the length of the separation zone better than some of the conventional EVMs. Figure 13 and Table 8 show that the most commonly used $k - \varepsilon$ model fails to capture the formation of the flow separation zone and the other EVM models underestimate the length of this zone. The numerical simulations of the flow inside the duct with a u-bend show that the sensitized models (SARCM, SSTCC and SSTCCM) are the closest to the experimental data in terms of the velocity profile as well as the prediction and location of the separation zone.

Table 8: Location and length of the flow separation in the duct with a u-bend.

| | $k - \varepsilon$ | $k - \omega$ | SA | SST | SARCM | SSTCCM | SSTCC | Exp |
|---------------------------------|-------------------|--------------|-------|-------|-------|--------|-------|-------|
| location | - | π | π | π | π | π | π | π |
| length(x/H) | - | 0.4 | 0.54 | 0.8 | 1.15 | 1.78 | 1.78 | 1.5 |

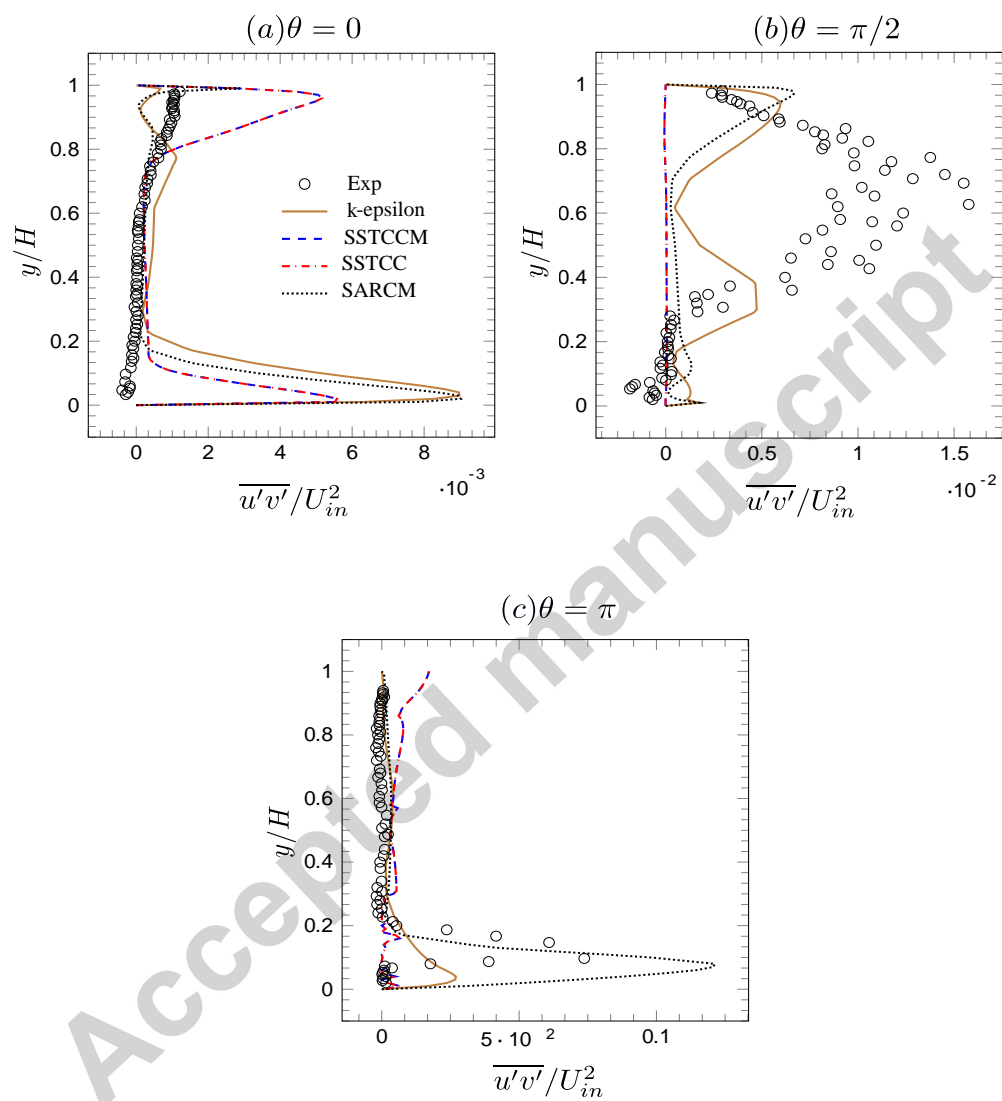


Figure 11: Reynolds shear stresses profile at $\theta = 0$, $\theta = \pi/2$ and $\theta = \pi$; comparison between the EVMs simulation and the LDA measurements.

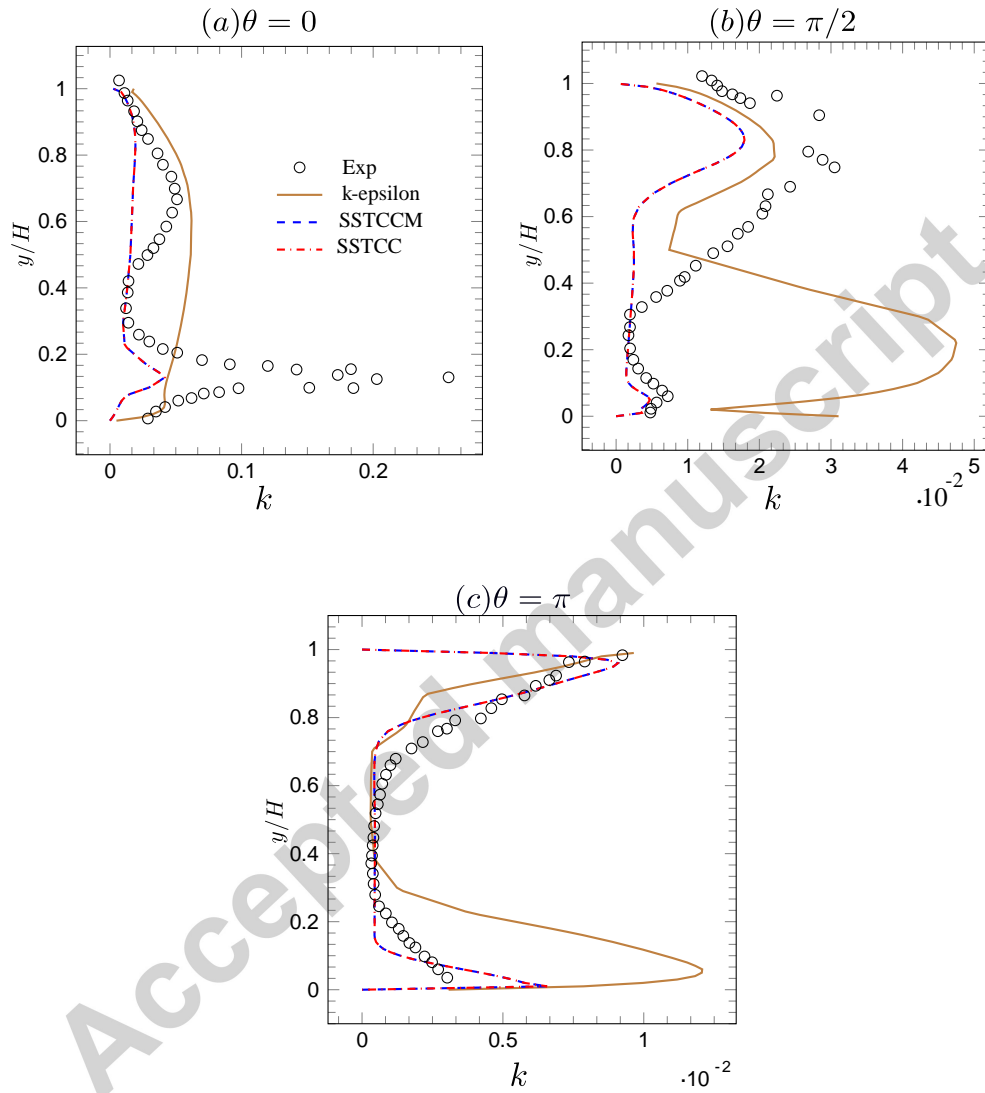


Figure 12: Turbulent kinetic energy profile at $\theta = 0$, $\theta = \pi/2$ and $\theta = \pi$; comparison between the EVMs simulation and the LDA measurements.

epsilon mg

SST

epsilon sAR

SSTCC

SMkC-

SSTCC-

Figure 13: Streamlines of the mean velocity of the flow within the U-duct for different EVM models.

5.2. Flow in a cyclone separator

It was found that the ability to correctly reproduce the flow at a horizontal cross section is the most severe test for turbulence models and consequently an important criterion for their selection. The models that passed the U-duct channel flow test were subsequently examined at this critical horizontal section. This assisted in identifying the best candidates in terms of turbulence models in further detail studies. In this section the values of the calculated velocities in the 3D Cartesian coordinate system frame are transformed into the tangential and the axial velocity components and are presented.

5.2.1. Sensitivity of the outlet boundary conditions on the flow

In this section, the proposed SSTCCM model is used to test the sensitivity of numerical solution in the flow domain to the imposed outlet boundary conditions. It is found that the boundary conditions at the apex outlet affect the accuracy of the obtained solution significantly. This is a consequence of two key factors; 1) the high possibility of a large gradients zone in the direction normal to the apex outlet, and 2) an outlet back-flow which could interfere with the flow inside the domain. Figure 14 shows the contour plots of the primitive variables (the velocity components and the static pressure) in the standard and extended geometry. This alternative geometry is extended by attaching a cylindrical element that is of a length equal to the body diameter of the cyclone at the end of the apex. This extension is necessary so that the numerical results could be compared with the available experimental results in [25]. The effects of the outlet boundary conditions in these two geometries are manifested in a different character of the flow variables. For instance, the tangential velocity contour shows that the standard and extended geometry preserve the Rankine pattern of the swirl velocity throughout the cyclone body. On the other hand, there is a dramatic change in the contour of the axial velocity between these two geometries.

Figure 15 shows the tangential velocity profile at different longitudinal levels. The Z-locations of these levels are presented previously in Fig. 8 and are consistent with the measurements reported in [25]. The readings are taken at two cross-sectional levels inside the barrel portion and at two levels inside the conical portion. Although the application of the

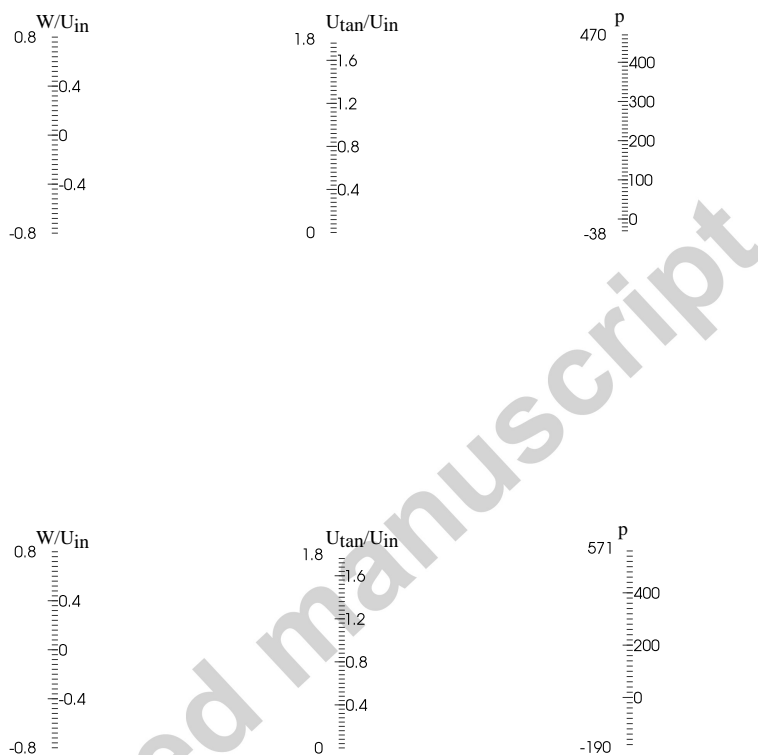


Figure 14: Contour plots of the flow variables at sections $Y = 0$. The standard Stairmand cyclone is shown at the top and the cyclone with extended outlet at the bottom. From left to right; the axial velocity, tangential velocity and the static pressure.

proposed model with the Neumann boundary conditions to the standard geometry preserves the Rankine pattern of the tangential velocity, the profile of the solid-body rotation is less accurate when compared to the extended one with the same boundary conditions.

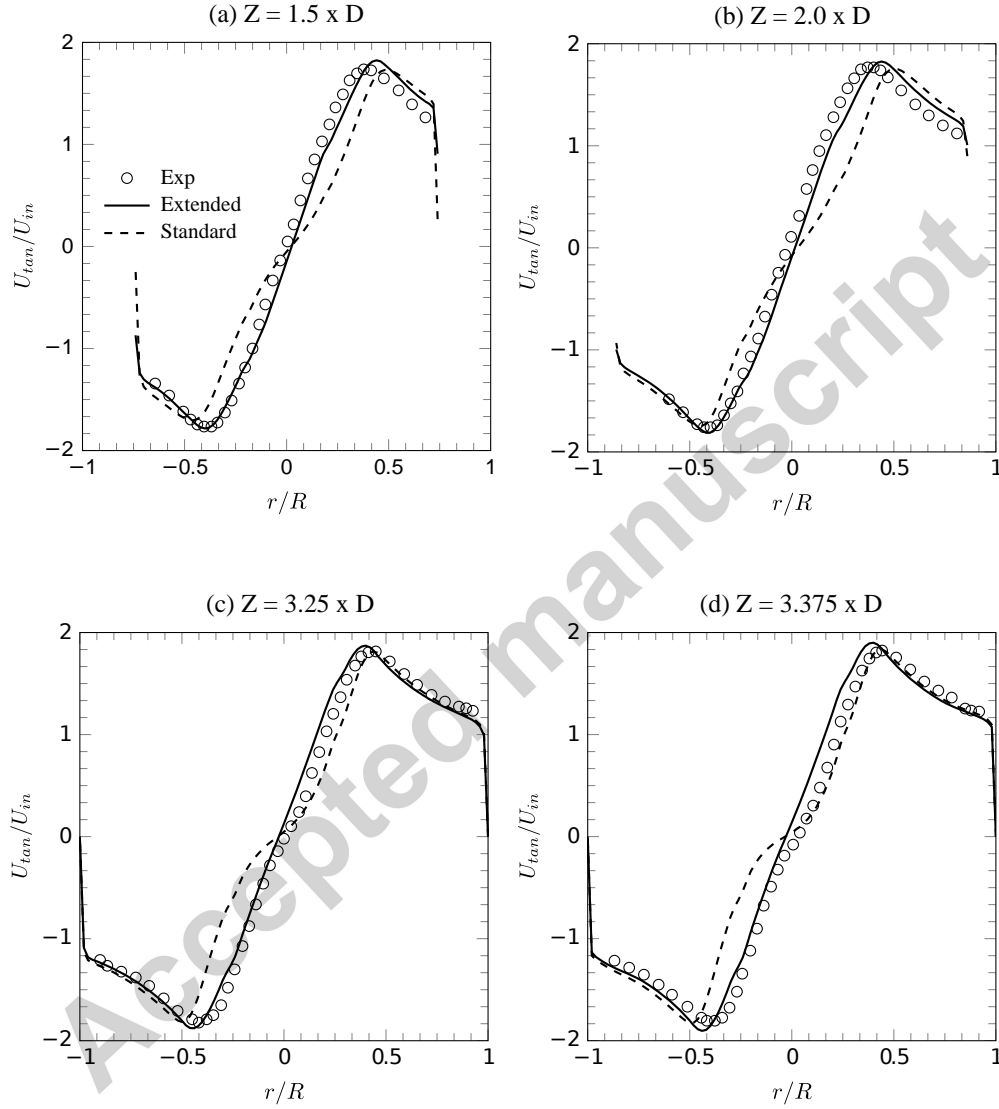


Figure 15: Comparison of the tangential velocity profiles between the extended and standard geometry at different levels.

In Fig. 16, the axial velocity profile of these two geometries is presented. It is found that the effect of the outlet boundary conditions on the axial profile is more significant

in the conical portion. The obtained results presented in Fig. 16c and d show that both geometries inside the separation section are in a good agreement with the experimental data. However, the normal geometry provides an inverted V pattern profile in the conical section, as shown in Fig. 17a and b. On the other hand, extending the outlet apex further reduces the effects of the applied boundary conditions at the apex surface. This is a necessary step in reducing the influence of the boundary conditions on the flow character and ensuring that the same physical behaviour takes place in both the experimental and numerical tests. This guarantees that the profile of the axial velocity component with the inverted W pattern is observed at both cross sections inside the conical part of the device. Therefore, the results presented in section 5.2.2 are based on the extended geometry.

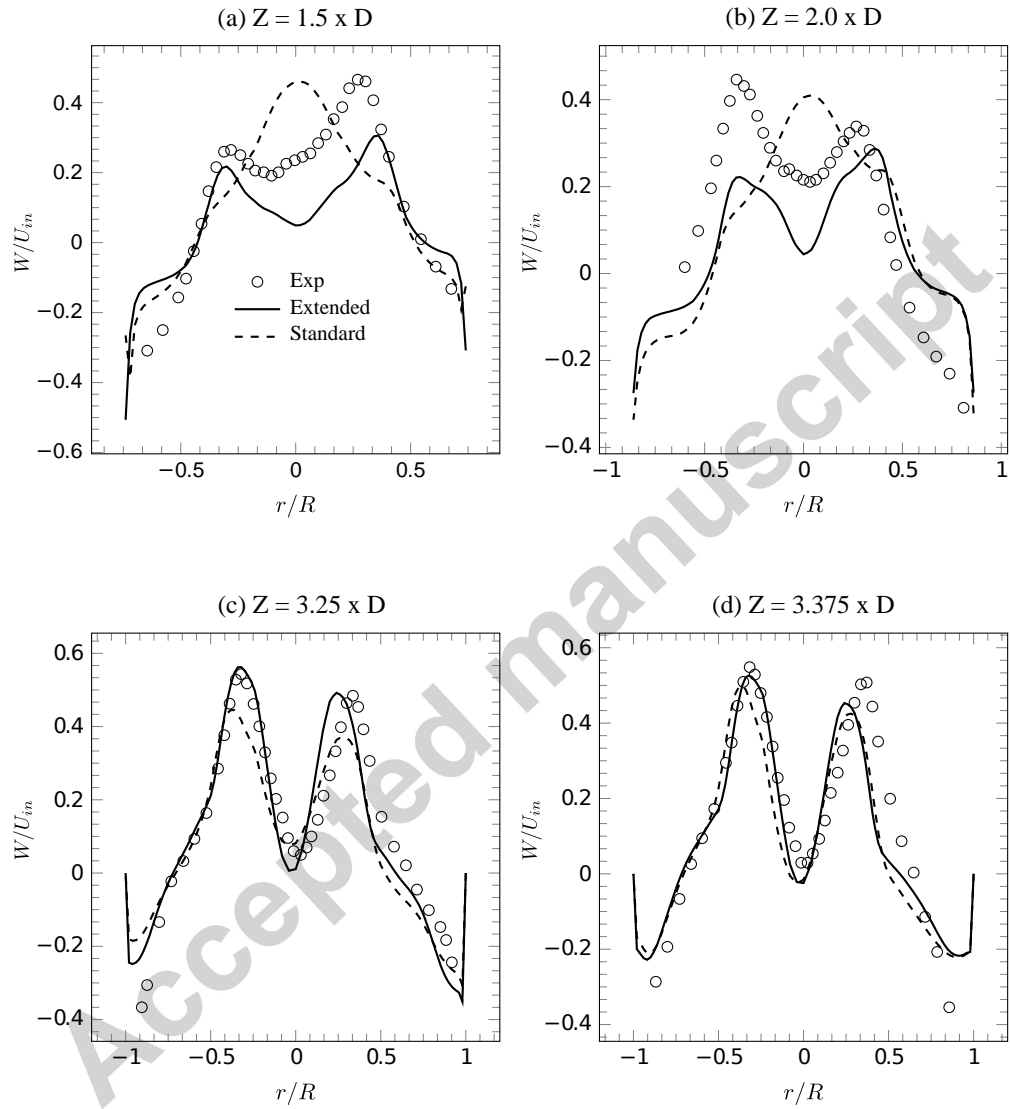


Figure 16: Comparison of the axial velocity profiles between the extended and standard geometry at different levels.

5.2.2. Swirling flow and turbulence model

The tangential velocity profile in a cyclone separator is generally described by the Rankine vortex structure, which is a combination of a solid-body and a free-vortex rotation (see discussion and Fig. 2 in Section 2). For instance, in the core region, the flow is dominated by the solid-body rotation, while the free-vortex type of rotation appears in the outer region. From previous studies on wall bounded swirling flows, the conventional EVMs are known for their inability to predict the Rankine vortex profile (see e.g. [27], [28] and [29]). Figure 17a demonstrates the radial distribution of the tangential velocity in a standard Stairmand cyclone at $Z = 3.25D$. It presents the results of the simulations which are performed using different turbulence models, i.e. the standard SST model, the SARCM model, the SSTCC model and the proposed SSTCCM model. The obtained results are compared with the RSM and experimental measurements of Heokestra [25]. It is seen that only the SSTCC and SSTCCM models are able to predict the Rankine vortex pattern in accordance with the experimental measurements.

The standard SST model underestimates the radial distribution of the tangential velocity over the entire diameter of the cyclone. As the SST model is based on the Boussinesq hypothesis, where the turbulent viscosity is of a scalar nature, it fails to predict the full structure of the Rankine vortex patterns.

The one-equation SARCM model shows some improvements over the standard SST model. This can be seen in the core region, where the solid-body type of rotation is accurately predicted. However, this model is still unable to represent the free-vortex type of rotation.

Figure 17b demonstrates the radial distribution of the axial velocity profile. According to several publications ([18], [30] and [25]), the inverted W pattern of the axial velocity in the cyclone cannot be predicted when the modelling assumptions are based on the EVMs. The SST model is consistent with these studies and fails to capture the axial velocity profile. On the other hand, all models sensitized to rotation and curvature effects are capable of predicting the inverted W shape pattern. However, the shape of the axial velocity profile obtained with the SARCM model has a downward peak value located halfway between the

vortex finder and the cyclone wall. This prediction is not confirmed by experimental results, which were reproduced using the proposed SSTCCM and the SSTCC models. Also, it underestimated the peak values of the upward axial velocity. On the contrary, the proposed model shows a significant improvement in predicting all three regions composing the axial velocity profile in the cyclone. The downward direction which starts and ends at the edge of the vortex finder. The two upward direction regions occur between the body wall and the vortex finder wall. Both the locations and the magnitudes of these three profiles are accurately presented by the SSTCC and SSTCCM models. It can be seen that similar velocity profiles were obtained from these two models. All the simulations were performed on an 8 nodes CPU 64 Linux machine using OpenFoam-2.4.0. The total CPU time necessary for the realisation of the computations with SSTCC was 13 hours and 18 minutes while it needed less time, 12 hours and 14 minutes, for the SSTCCM case.

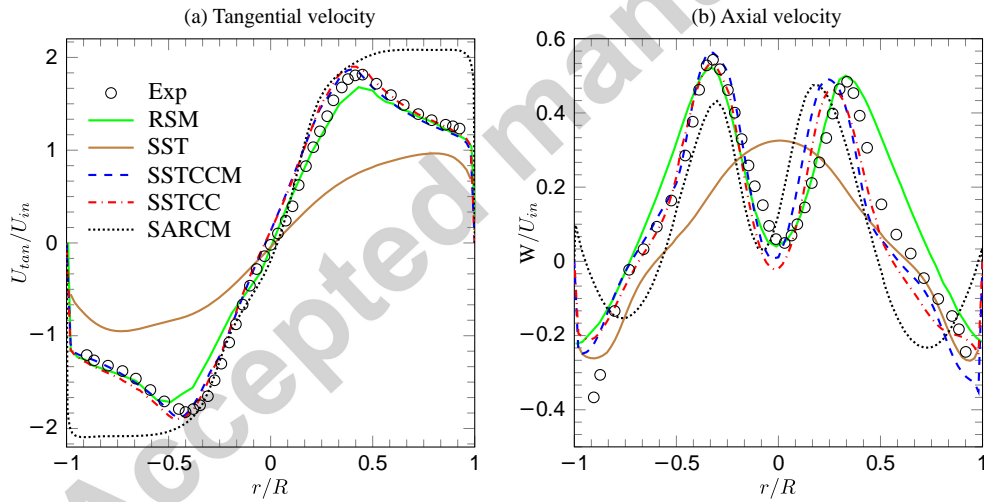


Figure 17: Comparison of the tangential velocity profiles (a) and axial velocity profiles (b) between the LDA measurements, RSM and the EVMs simulations with and without the curvature correction.

5.2.3. Cyclone performance and efficiency

The efficiency of the cyclone separator is obtained by measuring two parameters, i.e., the collection efficiency and the pressure drop. The centrifugal force is the main factor that drives the particles toward the wall and then they spiral down to the apex. According to Newton's second law of motion, the magnitude of the tangential inlet velocity is proportional to the centrifugal force acting on the solid particles. On the contrary, the pressure drop and consequently the operational cost of the cyclone rises proportionally to the inlet velocity. Therefore, the present study, focusing on accurately computing the swirling flow in the cyclone, is concluded by providing the performance information, which is further verified by the experiment.

The collection efficiency in this study is calculated by implementing the discrete phase modelling approach (DPM) to track the injected particles. The considered particles are of various sizes and the Rosin-Rammler technique was applied for their initial distribution. The maximum diameter was 1×10^{-5} m, and the minimum diameter was 1×10^{-7} m. The mean diameter was calculated from Fig. 18 and is approximately 3.4×10^{-6} m, while the average spread parameter is 1.675. The DPM was performed with a total flow rate of 0.001 kg/s and the maximum number of steps was 200,000.

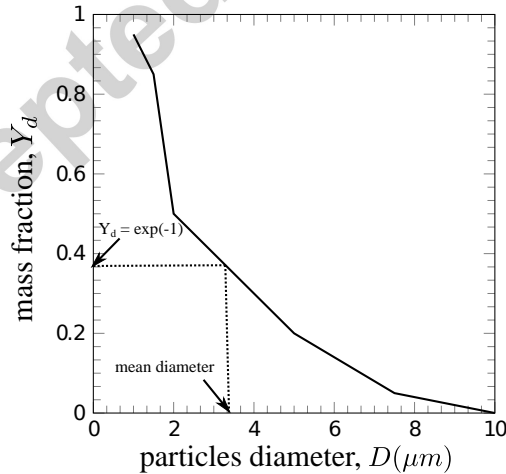


Figure 18: Cumulative size distribution of particles.

The particles were injected from the inlet surface with a velocity equal to the gas phase.

The collection efficiency curve presented in Fig. 19 is drawn from the statistical data of the monitored particles. All of the particles that flow through the apex outlet are considered as collected particles, while the escaped particles are those that flow through the top outlet. Some of the particles were suspended inside the cyclone and recirculated near the top wall of the barrel part. Therefore, the efficiency, η , is calculated using the following formula:

$$\eta = \frac{\text{trapped}}{\text{injected} - \text{suspended}} \quad (39)$$

The cut-off size diameter of the numerical results is approximately $1.4 \mu\text{m}$, which is reasonable compared to the $1.0 \mu\text{m}$ of the experimental calculation.

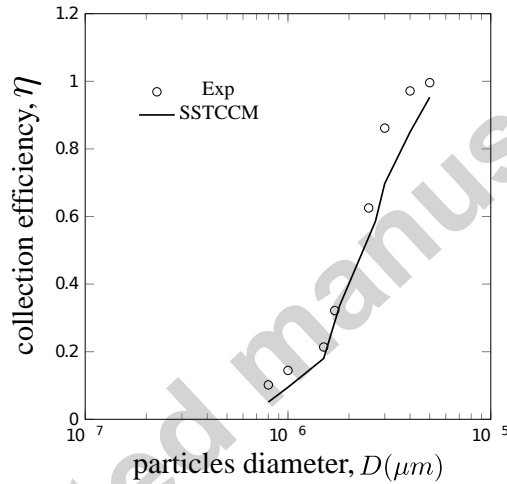


Figure 19: Grade efficiency curve of the proposed SSTCCM model compared to the experimental measurement.

The total pressure drop in the cyclone device is a combination of three major losses; losses in the inlet section, losses in the vortex finder and apex exit duct and losses resulting from the wall friction and irreversible losses within the vortex separation core. The latter has the major influence on the total pressure drop. The proposed model underestimated the pressure drop by approximately 8%. The Euler number and cut-off diameter X_{50} of the experimental and numerical results are depicted in Table 9.

Table 9: Pressure drop and the cut-off diameter of the proposed turbulence models and the experimental measurements of Hoekstra [25].

| | Euler number | X_{50} μm |
|------------|---------------------|------------------------|
| Experiment | 5.1 | 1.85 |
| SSTCCM | 4.8 | 2.39 |

6. Conclusion

A modification of the shear stress transport model with curvature correction, known as SSTCC model [3], was proposed. The primary aim of this work was to create a new model which does not contain the complex Lagrangian derivative term, which appears in equation (35). This term is replaced by the term representing the Richardson number, which leads to a simpler rotation/curvature correction method.

The modified eddy viscosity turbulence models (SARCM, SSTCC and the proposed SSTCCM) were employed to test the ability to simulate a highly swirling turbulent flow within a Stairmand high efficiency cyclone. This is the first time that these models were implemented to simulate the cyclone flow. A very good agreement was obtained between the numerical predictions and the experimental data of Hoekstra [25]. However, it is found that the SARCM model fails to predict the tangential velocity in the loss-free vortex regime, while the proposed SSTCCM shows superior performance in terms of the accuracy of the estimation of this critical regime. This is confirmed not only when compared with experimental measurements but also with other high level modelling approaches such as RSM.

The major features of the proposed approach may be summarized by the following statements:

- For both investigated cases the SSTCCM model reproduces the flow profiles with higher accuracy than the SARC model.
- The ability to represent the Rankine vortex pattern in a swirling flow, which is reflected in a characteristic form of the tangential velocity profile. This ability proved to be the most challenging for all conventional EVMs.

- The ability to represent the inverted W pattern of the axial velocity in a Stairmand cyclone flow. This feature also proved to be challenging for all conventional EVMs.
- The SSTCCM model not only preserves the accuracy of its predecessor but also it increases the computational efficiency. It is found that the proposed model reduces the CPU time by approximately 8.15% when compared to the SSTCC model for the presented cyclone simulations. Such computational gains are especially important in a context of complex design studies that need finer meshes.

These features favourably classify the proposed technique as the robust numerical tool for simulating the complex swirling flow in cyclones. It seems that these conclusions could be further extended by saying that the SSTCCM model could be successfully applied to other case studies such as industrial axi-centrifugal compressors or other gas turbines of comparable characteristics.

- [1] H. J. Lugt, *Vortex Flow in Nature and Technology*, New York, Wiley-Interscience, 1983, 305 p. Translation. 1.
- [2] K. Elsayed, C. Lacor, The effect of cyclone vortex finder dimensions on the flow pattern and performance using LES, *Computers and Fluids* 71 (2013) 224–239.
- [3] P. E. Smirnov, F. R. Menter, Sensitization of the SST turbulence model to rotation and curvature by applying the Spalart–Shur correction term, *Journal of Turbomachinery* 131 (4) (2009) 1–8.
- [4] R. Hreiz, C. Gentric, N. Midoux, Numerical investigation of swirling flow in cylindrical cyclones, *Chemical Engineering Research and Design* 89 (12) (2011) 2521–2539.
- [5] J. Howard, S. Patankar, R. Bordyniuk, Flow prediction in rotating ducts using coriolis-modified turbulence models, *Journal of Fluids Engineering* 102 (4) (1980) 456–461.
- [6] A. Gooray, C. Watkins, W. Aung, Improvements to the k-epsilon model for calculations of turbulent recirculating flow, in: *4th Symposium on Turbulent Shear Flows*, Vol. 1, 1984, p. 18.
- [7] S. Park, M. Chung, Curvature-dependent two-equation model for prediction of turbulent recirculating flows, *AIAA Journal* 27 (3) (1989) 340–344.
- [8] P. Spalart, M. Shur, On the sensitization of turbulence models to rotation and curvature, *Aerospace Science and Technology* 1 (5) (1997) 297–302.
- [9] D. Knight, P. Saffman, Turbulence model predictions for flows with significant mean streamline curvature, *AIAA Paper* 258 (1978) 1978.
- [10] A. Hellsten, Some improvements in Menter’s k- ω SST turbulence model, *AIAA* 2554 (1998) 1998.

- [11] A. Khodak, C. Hirsch, Second-order non-linear $k-\varepsilon$ models with explicit effect of curvature and rotation, in: ECCOMAS Computational Fluid Dynamics Conference, 1996, pp. 690–696.
- [12] Q. Zhang, Y. Yang, A new simpler rotation/curvature correction method for Spalart–Allmaras turbulence model, *Chinese Journal of Aeronautics* 26 (2) (2013) 326–333.
- [13] A. C. Hoffmann, L. E. Stein, *Gas Cyclones and Swirl Tubes*, Vol. 2008, Springer, 2002.
- [14] Z. Liu, Y. Zheng, L. Jia, J. Jiao, Q. Zhang, Stereoscopic piv studies on the swirling flow structure in a gas cyclone, *Chemical Engineering Science* 61 (13) (2006) 4252–4261.
- [15] C. Shepherd, C. Lapple, Flow pattern and pressure drop in cyclone dust collectors, *Industrial & Engineering Chemistry* 31 (8) (1939) 972–984.
- [16] A. Ter Linden, Investigations into cyclone dust collectors, *Proceedings of the Institution of Mechanical Engineers* 160 (1) (1949) 233–251.
- [17] W. Peng, A. Hoffmann, P. Boot, A. Udding, H. Dries, A. Ekker, J. Kater, Flow pattern in reverse-flow centrifugal separators, *Powder Technology* 127 (3) (2002) 212 – 222.
- [18] A. Horvath, C. Jordan, M. Harasek, Influence of vortex-finder diameter on axial gas flow in simple cyclone, *Chemical Product and Process Modeling* 3 (1) (2008) 2008.
- [19] P. Spalart, S. Allmaras, One-equation turbulence model for aerodynamic flows, *Recherche Aeronautique* (1) (1994) 5–21.
- [20] F. R. Menter, Two-equation eddy-viscosity turbulence models for engineering applications, *AIAA Journal* 32 (8) (1994) 1598–1605.
- [21] C. Greenshields, *OpenFOAM user guide*, version 2.4.0 (2015).
- [22] L. Chen, J. Zang, A. Hillis, G. Morgan, A. Plummer, Numerical investigation of wave–structure interaction using OpenFOAM, *Ocean Engineering* 88 (2014) 91–109.
- [23] C. Geuzaine, J.-F. Remacle, Gmsh: A 3-D finite element mesh generator with built-in pre-and post-processing facilities, *International Journal for Numerical Methods in Engineering* 79 (11) (2009) 1309–1331.
- [24] M. J. Doby, W. Kraipech, A. F. Nowakowski, Numerical prediction of outlet velocity patterns in solid–liquid separators, *Chemical Engineering Journal* 111 (2) (2005) 173–180.
- [25] A. J. Hoekstra, Gas flow field and collection efficiency of cyclone separators, Ph.D. thesis, TU Delft, Delft University of Technology (2000).
- [26] D. Monson, H. Seegmiller, P. McConnaughey, Comparison of experiment with calculations using curvature-corrected zero and two equation turbulence models for a two-dimensional u-duct, in: *AIAA*, no. 90-1484., 1990.
- [27] S. Mousavian, A. Najafi, Numerical simulations of gas–liquid–solid flows in a hydrocyclone separator, *Archive of Applied Mechanics* 79 (5) (2009) 395–409.

- [28] H. Shalaby, K. Pachler, K. Wozniak, G. Wozniak, Comparative study of the continuous phase flow in a cyclone separator using different turbulence models, *International Journal for Numerical Methods in Fluids* 48 (11) (2005) 1175–1197.
- [29] S. Fraser, A. Abdel-Razek, M. Abdullah, Computational and experimental investigations in a cyclone dust separator, *Proceedings of the Institution of Mechanical Engineers, Part E: Journal of Process Mechanical Engineering* 211 (4) (1997) 247–257.
- [30] M. Slack, R. Prasad, A. Bakker, F. Boysan, Advances in cyclone modelling using unstructured grids, *Chemical Engineering Research and Design* 78 (8) (2000) 1098 – 1104.

Accepted manuscript